### Title
Failure Mode of Lithium Metal Batteries with a Block Copolymer Electrolyte Analyzed by X-Ray Microtomography




### Journal
Journal of The Electrochemical Society, 162(7)

### ISSN
0013-4651



### Authors
Devaux, Didier
Harry, Katherine J
Parkinson, Dilworth Y
et al.



### Publication Date
2015

### DOI
10.1149/2.0721507jes

Peer reviewed

# Failure Mode of Lithium Metal Batteries with a Block Copolymer Electrolyte Analyzed by X-Ray Microtomography

**Didier Devaux,[a,*] Katherine J. Harry,[b,c] Dilworth Y. Parkinson,[d] Rodger Yuan,[a,b] Daniel T. Hallinan,[e] Alastair A. MacDowell,[d] and Nitash P. Balsara[a,b,c,f,**,z]**

[a]*Environmental Energy Technologies Division, Lawrence Berkeley National Laboratory, Berkeley, California 94720, USA*
[b]*Department of Materials Science and Engineering, University of California, Berkeley, California 94720, USA*
[c]*Materials Science Division, Lawrence Berkeley National Laboratory, Berkeley, California 94720, USA*
[d]*Advanced Light Source Division, Lawrence Berkeley National Laboratory, Berkeley, California 94720, USA*
[e]*Department of Chemical and Biomedical Engineering, Florida A&M University–Florida State University College of Engineering, Tallahassee, Florida 32310, USA*
[f]*Joint Center for Energy Storage Research (JCESR), Lawrence Berkeley National Laboratory, Berkeley, California 94720, USA*

Solid block polymer electrolytes are promising candidates for the development of high energy density rechargeable lithium metal based batteries. All solid-state batteries comprising lithium metal negative electrode and lithium iron phosphate ($LiFePO_4$) composite positive electrode were assembled. A polystyrene-*b*-poly(ethylene oxide) (SEO) copolymer doped with a lithium salt was used as the electrolyte. After cycling the batteries, the reason for capacity fade and failure was determined by imaging the batteries using synchrotron hard X-ray microtomography. These experiments revealed partial delamination of the lithium foil and the block copolymer electrolyte layer. The void volume between the foil and electrolyte layer obtained after 40 to 90 cycles is comparable to volume change in the battery during one cycle. A simple model to account for the effect of delamination on current density in the battery is presented. Capacity fade and battery failures observed in our experiments are consistent with this model. No evidence of lithium dendrite formation was found. In contrast, cycled lithium-lithium symmetric cells with the same polymer electrolyte at the same current density failed due to dendrite formation. No evidence of delamination was found in these cells.
 [DOI: 10.1149/2.0721507jes] 

Manuscript submitted February 27, 2015; revised manuscript received March 30, 2015. Published April 17, 2015.

Solid polymer electrolytes are promising candidates for the development of high performance rechargeable batteries comprising a lithium (Li) metal electrode due to their chemical stability toward lithium and their mechanical resistance to dendrite growth.[1–3] After the pioneering work by Fenton et al.,[4] where poly(ethylene oxide) (PEO) laden with alkali metal salts was shown to possess good ionic conductivity, its application as a polymer electrolyte in a full cell was demonstrated by Armand et al.[5–7] PEO is a semi-crystalline polymer at room temperature. Ionic transport in PEO electrolytes is linked to segmental motion of the polymer chains,[8,9] and occurs predominantly in the amorphous phase.[10] Thus solid polymer electrolyte based batteries must be operated at temperatures ($T$) above the PEO melting temperature. However, amorphous PEO is too soft to avoid short circuit due to lithium dendrite growth.[11,12] One approach for resolving this problem is the use of a block copolymer electrolyte.[13–22] Immiscibility between the blocks induces microphase separation, producing hard insulating phases interspersed with soft, ionically conductive phases.[23–25]

In studies utilizing block copolymers as solid polymer electrolytes, the mechanical phase is usually made of a high glass transition temperature polymer such as polystyrene.[26–29] Extensive work on the thermodynamics of polystyrene-*b*-poly(ethylene oxide) (SEO) diblock copolymers[30–33] indicate that the tendency for microphase separation is enhanced by the presence of ions.[34,35] For symmetric SEO electrolytes, i.e. copolymers wherein the volume fraction of the conducting phase is above 50%, the ionic conductivity has been shown to increase with PEO chain length until it plateaus when the number-averaged molecular weight ($M_n$) of the PEO block exceeds 100 kg/mol.[32] In contrast, the ionic conductivity of PEO homopolymer decreases with increasing molecular weight, reaching a plateau as the molecular weight of the PEO block exceeds 4 kg/mol.[8]

In addition to ionic conductivity, the performance of a battery depends on two additional electrolyte transport properties: the salt diffusion coefficient[36] which is about 8 $10^{-8}$ $cm^2/s$ and the cation transference number which has not yet been rigorously measured and is estimated to be between 0.1 and 0.2 based on preliminary data.[37] The numerical values reported in the previous sentence apply to high $M_n$ SEO copolymers. The electrochemical stability window of the electrolyte determine the potential of the battery.[6,38] The electrochemical stability window of PEO homopolymer doped with LiTFSI is about 4 V vs. $Li^+/Li$.[39] We expect the electrochemical stability window of SEO to be in the same range.[40]

The mechanical properties of solid polymer electrolytes are important for many reasons. The electrolyte must be rigid enough to stop dendrite growth during battery cycling, and withstand processing steps for mass production of the electrolyte films and battery assembly. In addition, the electrolyte must be compliant enough so that adhesive contact between the electrolyte and the electrodes is maintained during all stages of battery cycling. To our knowledge, there have been very few studies of adhesion between solid electrolytes (polymers, ceramics, glasses) and electrodes.[41,42]

Characterization and prevention of dendrites in lithium metal batteries is gaining increasing attention.[11,12,41,43–70] A powerful approach for studying dendrite formation is hard X-ray microtomography.[71] This technique is particularly well-suited to study pouch cells as dendrite growth can be characterized without taking the cell apart, thereby reducing the risk of deforming or destroying the delicate dendrites that form during cell cycling. In addition, hard X-ray microtomography creates a full three-dimensional reconstruction of the cell. The hard X-rays penetrate through the protective pouch material and illuminate the dendrites inside the cell. Hard X-ray microtomography studies on cycled symmetric lithium-lithium cells with a block copolymer (SEO) electrolyte showed that dendrites were not simply protrusions that puncture through the electrolyte, but that much of the dendritic structure lies within the lithium electrode.[71,72] In addition, it was observed that the interfaces between the lithium electrodes and the SEO electrolyte remain smooth and intimate throughout the cells. In other words, failure in cycled lithium-lithium symmetric cells was not due to the loss of adhesive contact between the electrode and the electrolyte.

In this paper, we present the first characterization of cycled full cells comprising a lithium metal negative electrode and an

*Electrochemical Society Student Member.
**Electrochemical Society Active Member.
zE-mail: nbalsara@berkeley.edu

SEO electrolyte using hard X-ray microtomography. The composite positive electrode used in this study contained lithium iron phosphate ($LiFePO_4$) particles as the active material mixed with SEO electrolyte and carbon black. The batteries were cycled at current densities between 0.024 and 0.163 mA/cm$^2$. In a previous publication, Hallinan et al.[40] reported on the cycling stability of similar batteries but at higher current density (0.175 mA/cm$^2$). In both cases, batteries were cycled at 90°C to prevent crystallization of the PEO block. At this temperature, the polystyrene is close to a glass transition and the measured low frequency shear modulus of the SEO electrolyte is 1.1 $10^7$ Pa.[72] This is a factor 545 lower than the theoretically predicted modulus required to prevent dendrite growth from lithium metal electrode.[73] The observed failure in batteries in Ref. 40 was thus attributed to lithium dendrite growth. Our use of hard X-ray microtomography in the present study enables direct identification of the failure mode in these batteries. Surprisingly, no evidence of lithium dendrite growth was found. Failure occurs due to loss of adhesive contact between the lithium metal electrode and the SEO electrolyte.

## Experimental

*Electrolyte preparation.*— The polystyrene-*b*-poly(ethylene oxide) (SEO) block copolymer was synthesized by sequential anionic polymerization and characterized using methods described previously.[28,30] The number-averaged molecular weights ($M_n$) of the PS and PEO are 240 and 260 kg/mol, respectively, with an overall dispersity index of 1.23. In the SEO block copolymer, the PEO volume fraction is 0.51 and self-assembly results in the formation of a lamellar morphology.[28] Inside a MBraun glove box, maintaining an argon atmosphere with ultralow concentrations of water and oxygen, the block copolymer was first dried in the antechamber under vacuum at 90°C overnight, while the lithium bis(trifluoromethanesulfonyl)imide (LiTFSI, Novolyte) was dried in a same manner at 120°C for three days. Then, in the glove box, a mixture of SEO and LiTFSI was dissolved in N-methyl-2-pyrrolidone (NMP 99.5% under Argon, EMD) and stirred at 90°C for several hours. The molar ratio $r$ of lithium ions ($Li^+$) to ethylene oxide (EO) moieties in our electrolyte was 0.085.[30] When the solution was clear and homogeneous, it was cast on a 201 annealed nickel (Ni) foil (All Foils, Inc.) using a doctor blade (Gardco) and a home-built casting device with a heated stage. The electrolyte film was obtained by drying at 65°C for 12 h in the glove box. The resulting membrane was peeled off from the Ni foil and dried in the glove box antechamber under vacuum at 90°C overnight. On average, the SEO electrolyte thickness was 34 ± 11 μm, where the ± symbol corresponds to the standard deviation of measured values of all experimentally determined parameters.

*Lithium symmetric cell assembly.*— Inside the glove box, 1.43 cm diameter disks of the dry electrolyte were punched from the electrolyte films. The electrolyte disks were placed in between two 1.1 cm diameter lithium disks cut from a 150 μm thick lithium foil (FMC). Then the entire assembly was gently pressed. A Ni tab was taped on each Li electrode and the assembly was vacuum sealed (Packaging Aids Corp) in an aluminum-laminated pouch bag (Showa Denko).

*$LiFePO_4$ electrode preparation and battery assembly.*— The $LiFePO_4$ (P2 grade) active material was obtained from Phostech Lithium and dried in the glove box antechamber at 120°C for at least three days prior to use. Inside the glove box, SEO/LiTFSI solution at $r = 0.085$ in NMP was stirred at 90°C with $LiFePO_4$ and carbon black (Denka). The electrode formulation was 70 wt% $LiFePO_4$, 25 wt% SEO/LiTFSI ($r = 0.085$), and 5 wt% carbon black. The resulting slurry was then thoroughly mixed with a homogenizer (Kinematica) at 19,000 rpm. The slurry was then cast on a 20 μm thick electrochemical grade aluminum (Al) foil using a doctor blade and our home-built caster. The $LiFePO_4$ electrode was first dried overnight at 60°C, followed by further drying at 90°C in the glove box antechamber under vacuum for 12 h. On average, the $LiFePO_4$ loading was 3.3 ± 1.2 mg/cm$^2$ with an average thickness of 17 ± 6 μm. Inside the glove box, a 1.1 cm diameter disk was punched from the $LiFePO_4$ electrode and pressed at 90°C and 29,000 psi several times to reduce electrode porosity that formed during the casting process. The electrode was hand-pressed at 90°C onto a 1.43 cm diameter electrolyte disk. Then a 1.27 cm diameter lithium disk was gently pressed onto the SEO electrolyte. Aluminum and Ni tabs were taped on the $LiFePO_4$ and lithium electrodes, respectively, and the assembly was vacuum sealed (Packaging Aids Corp) in an aluminum-laminated pouch bag (Showa Denko).

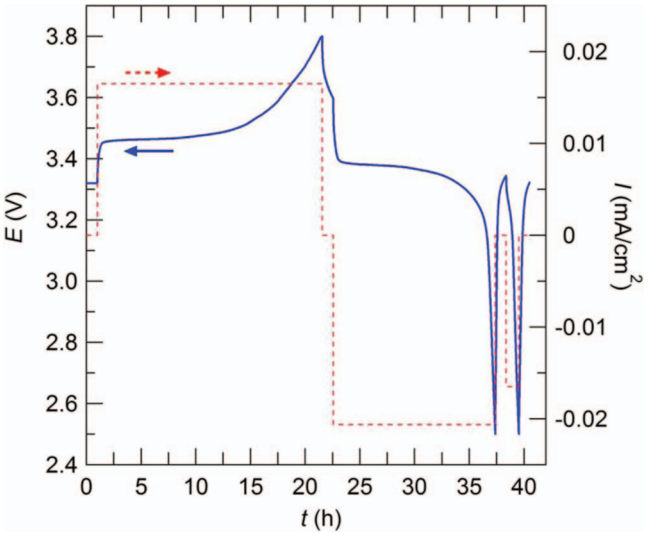


**Figure 1.** Battery cycling data (potential $E$ versus time) for a $C/20$ charge, $C/15$ discharge, followed by a second $C/20$ discharge. A 1 h rest period occurs in between each step.

*Battery and lithium symmetric cell cycling.*— After assembly inside the glove box, twelve battery replicates were transferred into a 90°C oven connected to a Maccor cycler where they were heated at 90°C overnight prior to any cycling. Due to the variation of thicknesses of $LiFePO_4$ electrodes and our limited accuracy of the balance used to weigh the $LiFePO_4$ electrodes, we were only able to obtain an approximate value for the $LiFePO_4$ loading in each battery. The battery cycling rate is reported in term of $C/n$ where $n$ is the number of hours used to either charge or discharge the battery. Five conditioning charge-discharge cycles were performed at an approximate rate of $C/20$, using the approximate $LiFePO_4$ loading described above. From these initial cycling results, a more accurate mass of $LiFePO_4$, $m_{LFP}$, in the positive electrode was determined by assuming that the measured battery capacity at this approximate $C/20$ rate is the theoretical capacity of $LiFePO_4$ (170 mAh/g). We refer to the capacity thus obtained as the practical capacity of the battery. The average difference between the approximate and practical capacities was 10 ± 5.3%. From this point forward, we only report the practical battery capacity. The batteries were cycled for 5 more cycles at the practical $C/20$ rate. Batteries were then charged at the $C$-rate of interest. Charging was done using a constant current, $I_c$, until the potential reached 3.8 V. This was followed by a constant voltage step at 3.8 V. This step was stopped when the current was 0.9 x $I_c$. After a 1 h rest period, a discharge current, $I_d$, was applied until the potential reached 2.5 V. After another 1 h rest period, another $C/20$ discharge step was executed until the potential reached 2.5 V. Typical charge-discharge data are shown in Figure 1 where battery potential, $E$, obtained during the charging, discharging, and rest steps is plotted versus time for a $C/15$ experiment. The final discharge step is conducted to distinguish between capacity fade at a given $C$-rate due to transport limitations within the $LiFePO_4$ electrode and that due to irreversible changes in the battery.

For each cycle, the charge ($Q_c$) and discharge ($Q_d$) capacities normalized by the estimated mass of $LiFePO_4$, $m_{LFP}$, was calculated by integrating the current over time. From this point, the capacity values based on the mass of the $LiFePO_4$ are reported in mAh/g.

$$Q_c(I_c) = \frac{\int I_c \cdot dt}{m_{LFP}} \quad [1]$$

$$Q_d(I_d) = \frac{\int I_d \cdot dt}{m_{LFP}} \quad [2]$$

The Coulombic efficiency ($\eta$) is defined by:

$$\eta = \frac{Q_d(I_d) + Q_d(I_c)}{Q_c(I_c)} \quad [3]$$

The thickness of the lithium layer stripped and plated on the lithium metal during each cycle, $l$, is approximatively given by:

$$l = \frac{I \cdot t \cdot M_{Li}}{\rho \cdot F \cdot \pi \cdot R_c^2} \quad [4]$$

where $\rho$ is the density of lithium metal (0.534 g/cm$^3$), $F$ is the Faraday constant (9.648 $10^4$ C/mol), $R_c$ is the radius of the $LiFePO_4$ electrode (0.55 cm, the smaller of the two electrodes), $M_{Li}$ the lithium molar mass (6.941 g/mol) and $t$ the time of the charge or discharge step.

The performance of each battery was evaluated using two consecutive experiments. In the first experiment, the discharge capacity at different *C*-rates was measured using a constant *C*/20 charge. After each cycle, the *C*/*n* discharge rate was increased by decreasing *n* ranging from 20 to 1/10 h. A final *C*/20 cycle was performed to quantify irreversible changes in the battery during this experiment. In the second experiment, the battery cycle life was determined at constant current density (about 0.052 mA/cm$^2$), using the cycle described above (two discharge steps). To establish the generality of our conclusion, batteries were cycled at either 0.024 mA/cm$^2$ (two step discharges) or at 0.163 mA/cm$^2$ (one step discharge).

Symmetric lithium cells were cycled using the same protocol described above. In this case, one cycle corresponds to 4 h charge and a 4 h discharge. A 45 min rest period was executed between each charge and discharge step. The cells were subjected to 15 conditioning cycles at a current density of 0.02 mA/cm$^2$, and then cycled at 0.104 mA/cm$^2$ until failure using the Maccor cycler at 90°C. The thickness of the lithium layer transported during each charge-discharge cycle is about 2 μm in both symmetric cells and batteries.

*Hard X-ray microtomography.*— After lithium symmetric cell and battery cycling, the cells were taken back to the glove box for disassembly. The cells were opened and the tabs were removed. For each cell, a 3 mm diameter punch was used to cut a portion of the cell. This portion was resealed under vacuum in a pouch bag.[71] The same procedure was used to prepare samples of uncycled lithium symmetric cells and batteries that were heated overnight at 90°C. The samples were then transferred to the hard X-ray microtomography beamline 8.3.2 at the Advanced Light Source at the Lawrence Berkeley National Laboratory.[74] The samples were illuminated using monochromatic hard X-rays of 25 keV energy. The samples were imaged at either room temperature or at 90°C, using a copper heating element located under the cell. The X-rays radiogram was converted into visible light using a 50 um thick LuAG scintillator. An optical microscope equipped with a sCMOS camera was used to magnify the images and convert them into digital image files. A 10× lens was used in the optical microscope, resulting in images with square pixels of length 0.64 μm. 1025 images were collected from the sample as it was continuously rotated through 180°. After a series of data processing steps, these radiograph images were converted to cross-sectional slices that were stacked to create a 3D reconstruction of the cell. Reconstructions were visualized and analyzed using the Avizo software package.

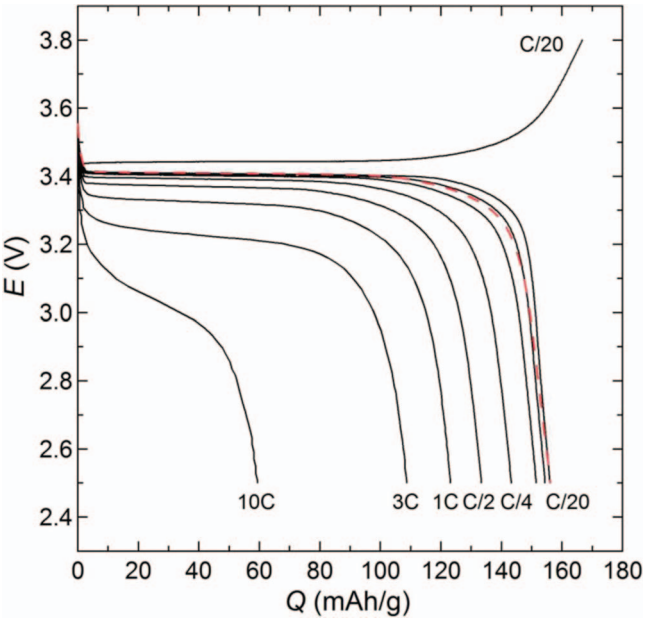


**Figure 2.** Battery potential, *E*, as a function of capacity, *Q*, at 90°C of a typical battery at selected *C*-rates. Charging was done at a constant rate (*C*/20) while the discharge rate was increased from *C*/20 to 10*C* before returning to a *C*/20 rate (dotted red line). The *C*/12 and *C*/8 discharge curves are not labelled for clarity.

## Results and Discussion

Typical results obtained during the first experiment wherein the discharge rate was increased from *C*/20 to 10*C* are presented in Figure 2 which shows the battery potential as a function of charge and discharge capacity. Only the first discharge is shown in Figure 2; the second *C*/20 discharge step is not shown for clarity. All the charging are similar and we thus show only one that exhibit a 3.44 V plateau as expected for an $LiFePO_4$ electrode. The average charge capacity obtained per cycle is 167.8 ± 1.4 mAh/g. The average discharge capacity decreases slightly from 157 to 144 mAh/g between *C*/20 and *C*/4, and the expected 3.40 V plateau is observed.[75] For higher discharge rates, the capacity drops rapidly from 134 mAh/g at *C*/2 to 59.4 mAh/g at 10*C*. This is accompanied by a decrease in the potential plateau from 3.37 V at *C*/2 to 3.2 V at 3*C*. For a discharge rate of 10*C*, polarization effects dominate and a well-defined potential plateau is not observed.[76] After this cycling procedure, the battery was cycled at *C*/20 where a discharge capacity of 156.5 mAh/g was obtained, comparable to the initial *C*/20 discharge capacity of 157 mAh/g. The capacity of the last *C*/20 discharge was, on average, 7.4 ± 0.5% lower than that of the first *C*/20 discharge, based on eight replicates.

The average discharge capacity of eight batteries is plotted as a function of the discharge *C*-rate between *C*/20 and 17*C* on a semi-log plot in Figure 3. Such a plot is usually referred to as a modified Peukert plot. Two data sets from literature are also shown for comparison. Both are lithium metal polymer batteries comprising $LiFePO_4$ electrode. One data set corresponds to a PEO composite electrolyte[77] at 76°C while the other one is a single-ion triblock copolymer electrolyte at 80°C.[3] At low *C*-rates, between *C*/20 and *C*/4, the average discharge capacity of our SEO batteries decreases from 157.6 ± 3.7 to 143.3 ± 5.5 mAh/g while the Coulombic efficiency remains higher than 98%. In this range of *C*-rates, the capacity retention is 91%. Moreover, in this *C*-rate range, the SEO based battery discharge capacities are close to the ones obtained with the single-ion copolymer electrolyte. The single-ion copolymer electrolyte represents the state-of-the-art polymer electrolyte for lithium metal battery as the capacity retention between *C*/15 and *C*/2 is 86% at 80°C. At higher *C*-rates, the discharge capacity falls rapidly down to 18 ± 2 mAh/g at 17*C* with an average Coulombic efficiency decreasing from 98% to 95%. The discharge

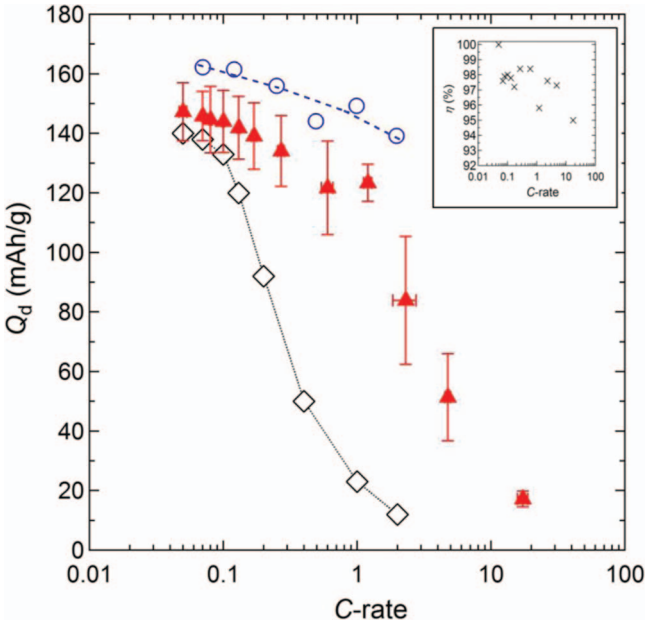


**Figure 3.** Modified Peukert plot of the specific discharge capacity, $Q_d$, as a function of *C*-rate for (▲) SEO electrolyte at 90°C (this work), (○) single-ion triblock copolymer electrolyte at 80°C taken from Ref. 3 and (◇) PEO composite electrolyte at 76°C taken from Ref. 77. The inset shows the average Coulombic efficiency η (×) as a function of *C*-rate. The average standard deviation of η is 1.8%.

capacity decay trend is similar to that of the PEO composite electrolyte. However, for the PEO composite electrolyte based battery, the sharp drops in capacity begins at *C*/10, and it reduces to 23 mAh/g at 1*C*.

The data in Figures 2 and 3 reflect the characteristic of our batteries during initial cycling. The main purpose of this paper is to study the effect of repeated cycling on the electrochemical characteristics of the batteries and morphology of the electrode and electrolyte layers. Eight full batteries were subjected to a long term cycling protocol, charging them at *C*/20 and discharging at *C*/8, with a subsequent *C*/20 discharge step, for up to 90 cycles. Figure 4 shows the potential profiles during charge and first discharge, as a function of the capacity at selected cycle numbers for two representative batteries, called battery A and B.

For battery A, Figure 4a, the charge and discharge capacity decrease continuously with increasing cycle number. After 90 cycles, the discharge capacity decreased by a factor of about two relative to the initial capacity. The difference between the charge and discharge potentials at a given capacity increased with cycle number. After 90 cycles, a well-defined potential plateau was absent, indicating the presence of strong polarization effects. In contrast, the potential profile of battery B shown in Figure 4b is not significantly affected by cycle number in spite of the fact that the procedure used to create this battery was nominally similar to that used to create battery A. The other batteries that were examined, batteries C through H, exhibited potential profiles that were qualitatively similar to those shown in Figure 4. For completeness, these profiles are given in Figure S1 (see Supporting Information).

The capacity evolution for battery A and B are plotted in Figure 5 as a function of the cycle number, *N*. The *C*/20 charge, *C*/8 discharge and the sum of the two *C*/8 and *C*/20 discharges are provided on this figure as well as the Coulombic efficiency. Battery A, shown in Figure 5a, shows continuous capacity fade with an average loss of $0.43 \pm 0.3$ mAh/g per cycle. Battery B, shown in Figure 5b, was able to hold a *C*/8 discharge capacity of about 147 mAh/g for 60 cycles before starting to drop down to 143.6 mAh/g at cycle 74. For all of the batteries, the charge and discharge capacity evolution is similar

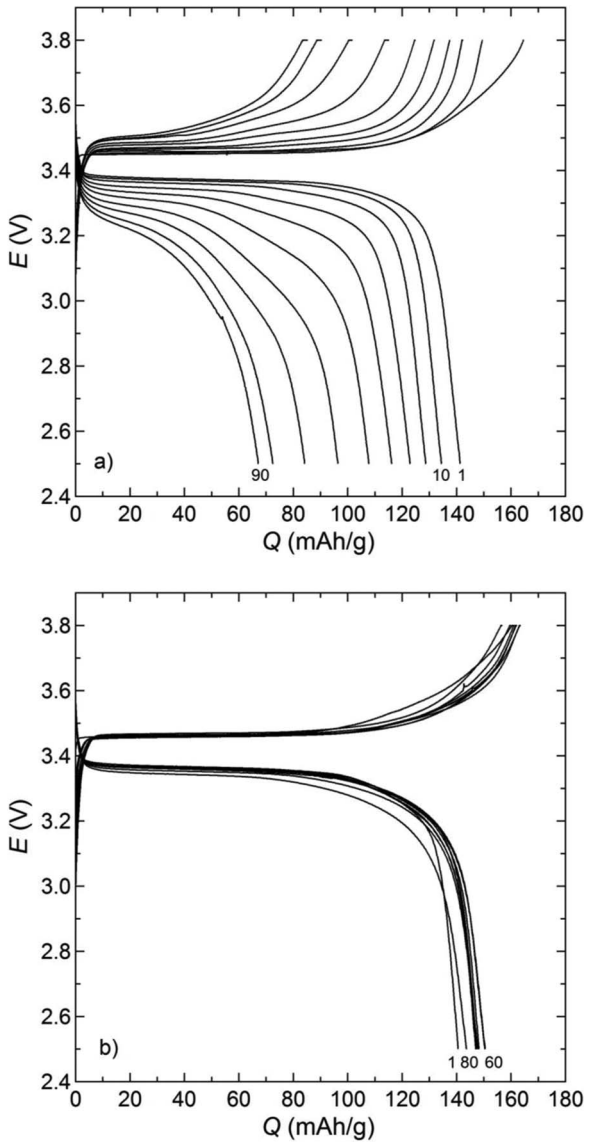


**Figure 4.** Potential, *E*, as a function of the specific capacity, *Q*, every 10 cycles at 90°C. a) battery A and b) battery B. The numbers under the discharge curves indicate the cycle numbers. The battery is charged at *C*/20 and discharged at *C*/8. For clarity, the second *C*/20 discharge at each cycle is not shown.

in trend. The average Coulombic efficiency at each charge-discharge cycle is $98.3 \pm 0.9\%$. The charge and discharge capacity changes with the cycle number of batteries C through H are given in Figure S2. These batteries follow the general trends depicted in Figure 5.

In an attempt to understand the cause of the capacity fade reported in Figure 5, the batteries were imaged by hard X-ray microtomography. (Due to limited access to the microtomography beamline only seven out of the eight batteries, A through G, were imaged.) In particular, we are interested in explaining the reason for the qualitative differences between batteries A and B seen in Figures 4 and 5 in spite of the fact that the processes used to make them were identical. For reference, three batteries were assembled and heated at 90°C and imaged directly without cycling to determine the initial state. Figure 6 shows microtomography cross-sections of batteries obtained at room temperature. Figure 6a shows an image of an uncycled battery. We see four distinct layers in intimate contact with each other: Li, SEO, $LiFePO_4$ composite electrode, Al current collector. (Only a small portion of the 150 μm thick Li electrode is shown.) The cross-section image of battery A and B, after being cycled at *C*/20 in charge and

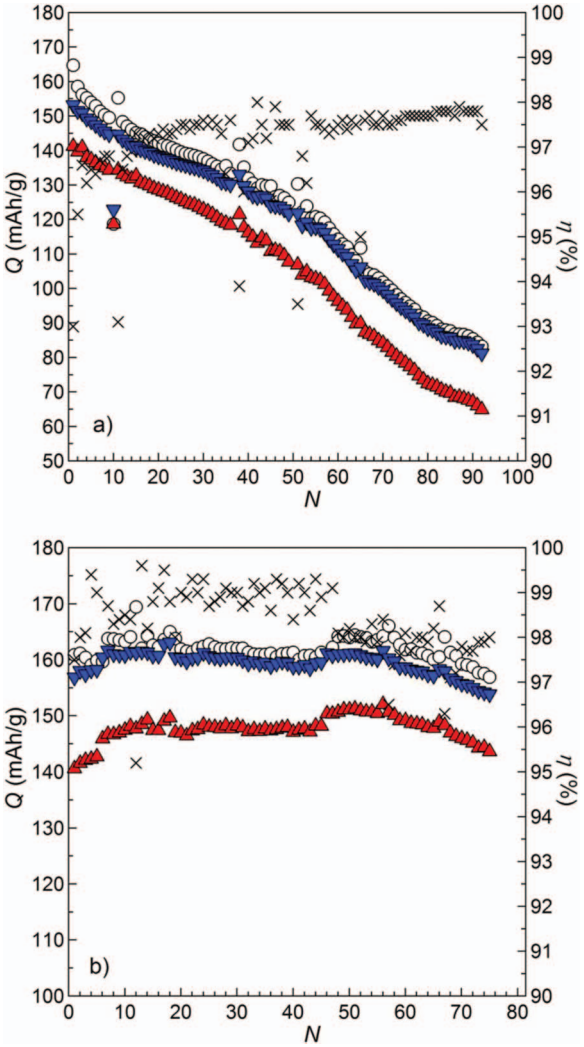


**Figure 5.** Specific capacities, *Q*, as a function of the cycle number, *N*, for a) battery A and b) battery B at 90°C. The symbols correspond to (○) *C*/20 charge; (▲) *C*/8 discharge; and (▼) sum of the *C*/8 and *C*/20 discharge. The Coulombic efficiency η (×) is shown on the right axis.

*C*/8 in discharge are shown in Figure 6b and 6c, respectively. The $LiFePO_4$ electrodes of all batteries, A through G, were punched out of one sheet while the electrolytes used in these batteries were punched out of different sheets. It is evident in Figure 6 that the $LiFePO_4$ electrode thicknesses are reasonably constant from battery to battery while the electrolyte thicknesses are not. The grayscale pixel values in Figure 6 correspond to the relative X-ray linear absorption coefficients of the material at that position – brighter pixels correspond to higher X-ray absorption at that position. Thus, the $LiFePO_4$ electrodes appear bright in Figure 6 because they are less X-ray transmissive. The lithium-electrolyte interface in Figure 6a is embellished by a thin dark band on the electrode side and a thin bright band on the electrolyte side; this is a result of Fresnel phase contrast arising during the imaging of samples containing interfaces.[72,78] The main difference between the cycled and uncycled batteries is that in addition to the Fresnel contrast band, darker structures appear at the lithium-electrolyte interface in the cycled batteries (Figure 6b and 6c). The measured X-ray absorption coefficient in this band is significantly lower than that obtained in the uncycled batteries. This difference is visualized in Figure 7. Using the Avizo software package, voxels with brightness below a certain threshold, approximately the lowest value seen in the uncycled battery, are considered voids and are colored red. The projection of these voxels in the plane of the electrode-electrolyte

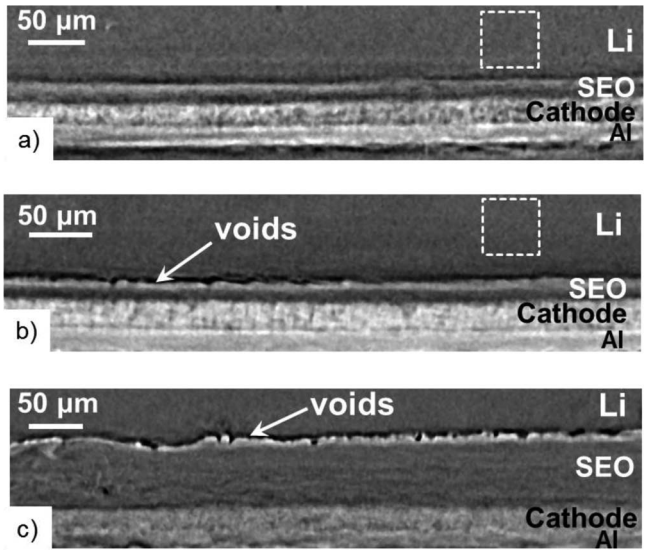


**Figure 6.** X-ray microtomography slices showing the cross-section of lithium metal polymer batteries at room temperature. a) uncycled battery annealed at 90°C; b) battery A after cycling; c) battery B after cycling. The dashed square shows the area used to normalize pixel intensity for thresholding calculations.

interfaces defined as the xy plane is shown in Figure 7. The qualitative differences between Figure 7a (uncycled battery) and Figure 7b (cycled battery A) indicates the development of a new feature at the lithium-electrolyte interface due to battery cycling. We note that to obtain the required resolution to see the voids in this experiment, we used a field of view which was smaller than the entire pouch containing the battery sample. This resulted in a slight shift in measured gray values in the reconstructed 3D images. To account for this, we normalized each image using as a standard regions of the image containing lithium metal. The intensity in the dashed square within the lithium metal in the two batteries shown in Figures 6a and 6b were averaged. The brightness of each voxel in the uncycled battery (Figure 6a) and the cycled battery A (Figure 6b) were normalized by these averages to account for differences in instrumental configurations used to obtain the tomograms. (The two samples were imaged during different runs.) The dark band in Figure 6b and 6c indicates the emergence of voids in those region, and thus delamination of the lithium and polymer electrolyte layers. It is interesting to note that delamination is seen in both battery A which exhibited significant capacity fade, and battery B which did not exhibit significant capacity fade. The reason for this will be discussed shortly. Delamination was also observed in batteries C through G (Figure S3). None of the tomograms showed any evidence of lithium dendrite formation.

The extent of delamination of the Li/SEO interface was quantified using the Avizo software package. After correcting the image gray values as described above, the void volume was digitally labeled or

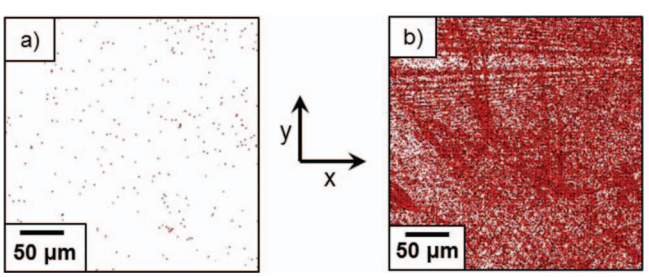


**Figure 7.** Projection of voxels with brightness below a fixed threshold value colored red in the plane of the electrode-electrolyte interfaces (xy plane). a) uncycled battery b) battery A after cycling. The red voxels represents voids determined by X-ray microtomography.

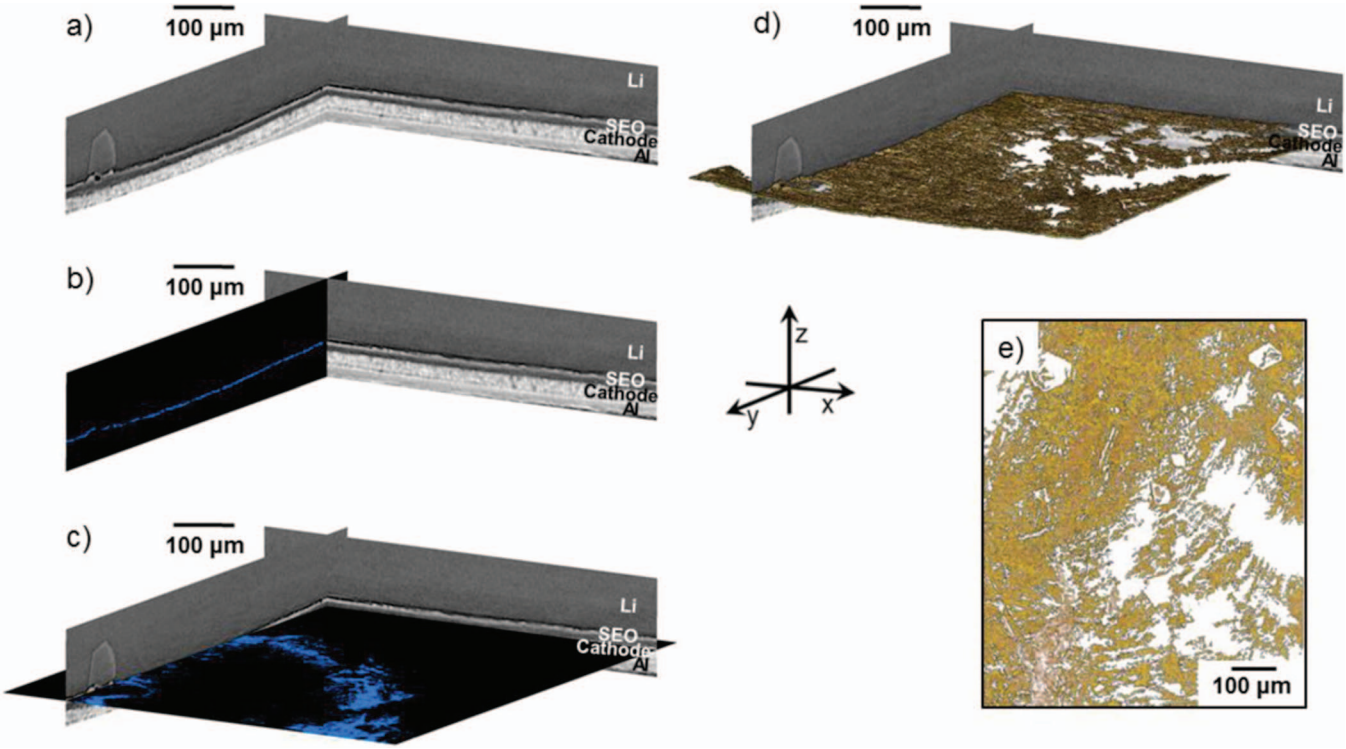


**Figure 8.** Microtomography image reconstruction of battery A and the segmentation method to estimate the fractional reduction in contact area due to cycling at the Li/SEO interface. a) X-ray microtomography slices showing the cross-section along the xz and yz planes; b) same as a) where the yz plane shows the voids segmented in blue; c) same as a) with one slice added along the xy plane showing the void segmented in blue; d) same as a) including the 3D reconstruction in yellow of the void at the Li/SEO interface and e) projected view of the 3D reconstructed void volume (yellow) and the Li/SEO interface point of contact (white).

"segmented" by selecting all voxels below an upper threshold of voxel brightness. Typical data obtained from battery A is shown in Figure 8. In Figure 8a we show two orthogonal slices through the battery along the xz and yz planes (coordinate system is defined in Figure 8). The result of segmentation on data in the yz plane is shown in Figure 8b where the void voxels are colored blue; all other voxels are colored black. The result of segmentation on data in the xy plane is shown in Figure 8c using the same color scheme. This enables the determination of the entire void volume between the lithium and electrolyte layers as shown by the yellowish voxels in Figure 8d. Projection of this volume in the xy plane is shown in Figure 8e using the same color scheme. The white region in Figure 8e thus represents regions where there is contact between the electrolyte and the lithium metal. Note the presence of polygonal white regions in Figure 8e due to the presence of crystalline impurities in the lithium metal reported previously in Ref. 71. The area fraction of white pixels in Figure 8e is defined as α. The procedure described here was repeated on batteries B through G and the results are presented in Table I (first seven entries). Values of α range from 0.29 to 0.46 with an average value of 0.37.

We propose that capacity fade is due to partial delamination at the Li/SEO interface. In our model, the effective surface area across which electrochemical reactions take place, $S_{\text{eff}}$, is given by:

$$S_{\text{eff}} = \alpha \cdot S \qquad [5]$$

We assume that no electrochemical reactions occur in portions of the cathode located directly across from the voids and thus, the effective *C*-rate in the presence of voids is $1/(\alpha \cdot t)$ where $t$ is the discharge time. Since our experiment is done at constant current,

**Table I. Characteristic of batteries cycled and imaged by X-ray microtomography.**

| Battery | Temperature* | Battery ending | Charge *C*-rate | Discharge *C*-rate | α** |
|---|---|---|---|---|---|
| A | R. T. | discharge | *C*/20 | *C*/8 | 0.31 |
| B | R. T. | discharge | *C*/20 | *C*/8 | 0.36 |
| C | R. T. | discharge | *C*/20 | *C*/8 | 0.39 |
| D | R. T. | discharge | *C*/20 | *C*/8 | 0.37 |
| E | R. T. | discharge | *C*/20 | *C*/8 | 0.29 |
| F | R. T. | discharge | *C*/20 | *C*/8 | 0.41 |
| G | R. T. | discharge | *C*/20 | *C*/8 | 0.33 |
| A | 90°C | discharge | *C*/20 | *C*/8 | 0.35 |
| I | R. T. | charge | *C*/20 | *C*/20 | 0.46 |
| J | R. T. | discharge | *C*/20 | *C*/20 | 0.46 |
| K | R. T. | charge | *C*/4 | *C*/4 | 0.37 |
| L | R. T. | discharge | *C*/4 | *C*/4 | 0.36 |

*R. T. for room temperature.
**α is the fractional contact area between the lithium electrode and the polymer electrolyte determined by tomography after cycling.

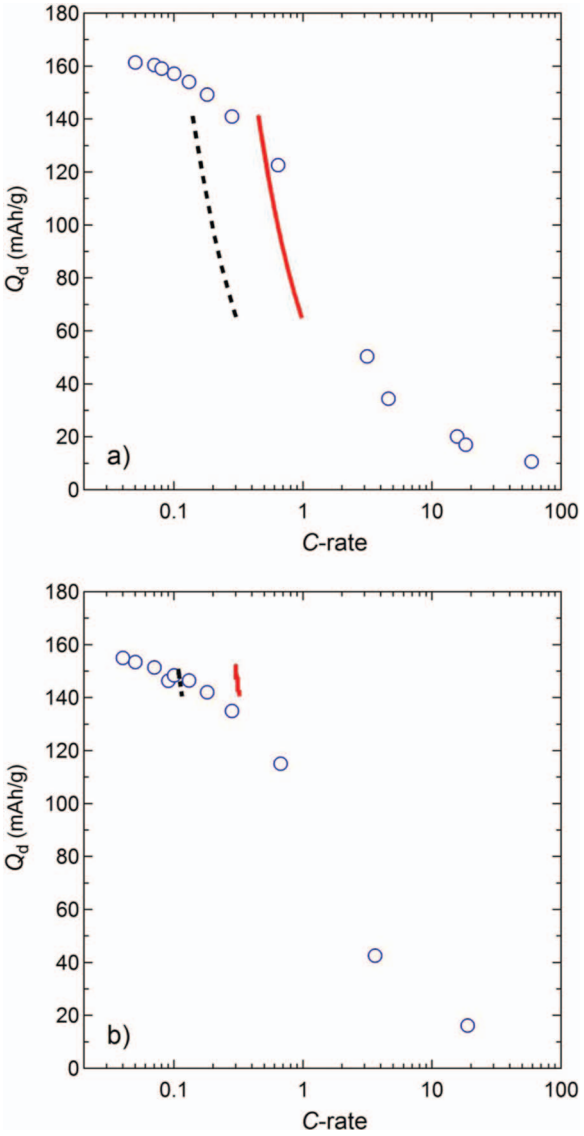


**Figure 9.** Quantification of capacity fade and battery failure. Measured discharge capacity, $Q_d$, of a) battery A and b) battery B as a function of *C*-rate. (- - -) *C*-rate; (—) effective *C*-rate using model that account for delamination. (○) modified Peukert plots of batteries A and B.

discharge time typically decreases with increasing cycle number due to capacity fade. The effective C-rate at all cycle numbers is increased by the same factor α.

Our model is illustrated in Figure 9. The dashed curves in Figure 9 represent the observed capacity fade of batteries A and B superimposed on their respective Peukert plots. For the battery A data with $\alpha = 0.31$ (see Table I), the effective *C*-rate at the first cycle is *C*/2.5. In a same manner, for battery B the effective *C*-rate is *C*/2.9. The solid curves in Figure 9a and 9b represent the observed capacity fade data of batteries A and B shifted horizontally by factor 2.5 and 2.9, respectively. The qualitative agreement between the shifted capacity fade data and the Peukert plot for both battery A and B (Figure 9) validates the proposed model and confirms the importance of void formation.

Table II summarizes the cycling characteristics of battery A through G. The data in this table correspond to portions of the batteries imaged by tomography. The volume of $LiFePO_4$ reported in Table II, $V_{LFP}$, is thus the amount active material in the full tomogram. Returning to Figure 8 where we show a few tomographic slices through battery A, $V_{LFP} = 1.74\ 10^6\ \mu m^3$ reported in Table II, represents an estimate of the amount of active material summed over all of the tomographic slices through battery A. This enables estimation of the amount of lithium, $l_{Li}$, deposited on the lithium electrode during the charging step at cycle one (before capacity fade). This value is also given in Table II. The difference in electrode volumes, $\Delta V$, in the charged and discharged batteries can then be calculated, given the density of lithium (0.534 g/cm$^3$) and differences in unit cell volumes of $FePO_4$ and $LiFePO_4$.[79] Table II also lists the void volume in each battery, $V_{void}$, obtained by X-ray tomography and the segmentation procedure outlined in Figure 8. The average value of $V_{void}/\Delta V$ is 2.3 ± 1.2 (see Table II). In other words $V_{void}$ and $\Delta V$ are comparable. It is likely that the voids seen in X-ray tomography occurred because of the inability of the block copolymer electrolyte to adhere to the lithium electrode as the electrodes shrink during discharging.

Our experiments so far do not shed light on either the formation of voids or on their evolution as battery is cycled. Obtaining this information will require in situ X-ray tomography experiments which are outside the scope of the present paper.

Our hypothesis is that the observed void formation is due to intrinsic difference in the volume of charged and discharged electrodes. Note that this difference is independent of *C*-rate in our experiment as we have used two discharge steps in our cycling procedure. We conducted several additional experiments to confirm the validity of our hypothesis. The batteries were cycled at 90°C while most of the imaging was done at room temperature. To ensure that this temperature difference was not affecting our results, several batteries, were imaged at 90°C. Typical results thus obtained are shown in Table I where we show value of α for battery A at 90°C, $\alpha = 0.35$. This compares well with value of α obtained for battery A at room temperature, 0.31. To ensure that void formation was not affecting by either charging rate or discharging rate, batteries I and J were charged and discharged at *C*/20, while battery K and L were charged and discharged at C/4. The charge and discharge capacity changes with the cycle number of batteries I through L are given in Figure S4. The decrease in capacity at C/20 is significantly lower than that at C/4. Batteries I and K were imaged after the charging step while batteries J and L were imaged after the discharging step. In spite of the differences in cycling history, the values of α obtained for these batteries

**Table II. Comparison of volume change per cycle and void volume of batteries.**

| Battery | A | B | C | D | E | F | G |
|---|---|---|---|---|---|---|---|
| $V_{LFP}$ ($\mu m^3$) | 1.74E + 06 | 1.93E + 06 | 4.02E + 06 | 3.03E + 06 | 2.98E + 06 | 4.09E + 06 | 1.76E + 06 |
| $l_{Li}$ (μm) | 1.90 | 1.60 | 2.05 | 1.54 | 2.15 | 2.82 | 2.12 |
| $\Delta V$ ($\mu m^3$) | 3.61E + 05 | 3.28E + 05 | 4.71E + 05 | 3.77E + 05 | 4.70E + 05 | 6.68E + 05 | 3.20E + 05 |
| $V_{void}$ ($\mu m^3$) | 1.41E + 06 | 3.49E + 05 | 1.45E + 06 | 1.05E + 06 | 1.47E + 06 | 9.22E + 05 | 2.46E + 05 |
| $V_{void}/\Delta V$ | 3.91 | 1.06 | 3.09 | 2.78 | 3.12 | 1.38 | 0.77 |

$V_{LFP}$ is the volume of $LiFePO_4$ in the full tomogram.
$l_{Li}$ is the amount of lithium deposited on the lithium electrode during the charging step at cycle one.
$\Delta V$ is the difference in electrode volumes in the charged and discharged batteries.
$V_{void}$ is the void volume in each battery obtained by X-ray tomography and the segmentation procedure outlined in Figure 8.

were similar to those reported previously battery A through G (see Table I).

Our work suggests that void formation between the lithium electrode and the SEO electrolyte play an important role in capacity fade of our batteries. Different batteries respond differently to the formation of voids due to the extremely nonlinear Peukert plot. Void formation does not affect batteries that start on the upper plateau of the Peukert plot while the performance of batteries that are located near the steep decline of the Peukert plot are more sensitive to void formation (see Figure 9). It is likely that other factors also affect cell performance. For example, we have not yet determined why some cells have large values of $\alpha$ (e.g. battery F) while others have a low value (battery E).

Lithium-lithium symmetric cells with the same polymer electrolyte at the same current density as that used during battery cycling (0.104 mA/cm$^2$) were cycled until failure and imaged by X-ray microtomography. In each cycle, the amount of lithium plated and stripped was equivalent to that of battery cycling. The results obtained were consistent with those reported in Refs. 40 and 71. No evidence of delamination was found in these cells, and cell failure was due to the growth of lithium dendrite, as established in the supporting information. Figure S5 shows microtomography cross-sections of the symmetric cells. Figure S5a shows an uncycled cell heated overnight at 90°C and imaged at room temperature. There is good adhesion between the electrodes and the electrolyte as was the case with uncycled battery (Figure 6a). Figure S5b shows microtomography cross-section of a failed cycled symmetric cell imaged at room temperature. Dendrites responsible for cell failure are clearly observed at the Li/SEO interfaces. The lack of delamination between the lithium electrodes and the SEO electrolyte seen in Figure 6b is similar to those reported previously.[71] Finally, the same failed lithium symmetric cell was taken back to the X-ray tomography beamline after several months of storage and imaged at 90°C. The result is presented in Figure S5c. It is evident that changing the cell temperature does not cause delamination.

We thus conclude that delamination seen in our batteries is due to the finite volume change of cycling. In the case of lithium symmetric cells, the volume change of cycling is zero and no delamination is observed. The failure mode of batteries and lithium symmetric cells are thus entirely different.

## Conclusions

Batteries comprising a lithium metal negative electrode, a solid block copolymer electrolyte, and an $LiFePO_4$ based positive electrode were cycled at 90°C at selected *C*-rates to determine the Peukert plot for each battery. This was followed by cycling at a constant current density to determine capacity fade and failure modes. Our experiments were restricted to current densities up to 0.163 mA/cm$^2$. After cycling, X-ray microtomography experiments revealed partial delamination of the interface between the lithium electrode and the solid polymer electrolyte. We propose that the decrease in contact area between the lithium electrode and the electrolyte due to delamination changes the effective *C*-rate of the batteries. The battery cycling data were consistent with a simple model that accounts for this effect using the Peukert plot of each battery. Lithium dendrites were not observed in the X-ray microtomography experiment on cycled batteries. In contrast, lithium-lithium symmetric cells with the same electrolyte, cycled at the same current density, and imaged by X-ray microtomography failed due to the formation of lithium dendrite. No evidence of delamination was found in the lithium-lithium symmetric cells. Further work is needed to study the evolution of voids, and to identify the current densities at which lithium dendrite grow in lithium-$LiFePO_4$ batteries with a solid block copolymer electrolyte.

## Acknowledgments

This work was primarily supported by the Joint Center for Energy Storage Research, an Energy Innovation Hub funded by the U. S. Department of Energy (DOE), Office of Science, Basic Energy Sciences (BES). The microtomography work was carried out at the Advanced Light Source at Lawrence Berkeley National Laboratory, which is supported by the Director, Office of Science, Office of Basic Energy Sciences, of the U. S. Department of Energy under Contract No. DE-AC02-05CH11231.

## References

1. J.-M. Tarascon and M. Armand, *Nature*, **414**, 359 (2001).
2. M. Armand, *Solid State Ionics*, **69**, 309 (1994).
3. R. Bouchet, S. Maria, R. Meziane, A. Aboulaich, L. Lienafa, J.-P. Bonnet, T. N. T. Phan, D. Bertin, D. Gigmes, D. Devaux, R. Denoyel, and M. Armand, *Nature Mater.*, **12**, 452 (2013).
4. D. E. Fenton, J. M. Parker, and P. V. Wright, *Polymer*, **14**, 589 (1973).
5. M. Armand, J. M. Chabagno, and M. J. Duclot, in *Fast Ion Transport in Solids Electrodes and Electrolytes*, P. Vashishta, J.-N. Mundy, and G. K. Shenoy, Editors, North-Holland, Amsterdam, p. 131 (1979).
6. M. Armand, *Solid State Ionics*, **9–10**, 745 (1983).
7. D. Baril, C. Michot, and M. Armand, *Solid State Ionics*, **94**, 35 (1997).
8. J. Shi and C. A. Vincent, *Solid State Ionics*, **60**, 11 (1993).
9. D. Diddens, A. Heuer, and O. Borodin, *Macromolecules*, **43**, 2028 (2010).
10. S. Lascaud, M. Perrier, A. Vallée, S. Besner, J. Prudhomme, and M. Armand, *Macromolecules*, **27**, 7469 (1994).
11. M. Dollé, L. Sannier, B. Beaudoin, M. Trentin, and J.-M. Tarascon, *Electrochem. Solid-State Lett.*, **5**, A286 (2002).
12. M. Rosso, C. Brissot, A. Teyssot, M. Dollé, L. Sannier, J.-M. Tarascon, R. Bouchet, and S. Lascaud, *Electrochim. Acta*, **51**, 5334 (2006).
13. T. Niitani, M. Shimada, K. Kawamura, and K. Kanamura, *J. Power Sources*, **146**, 386 (2005).
14. D. R. Sadoway, *J. Power Sources*, **129**, 1 (2004).
15. P. Jannasch, *Chem. Mater.*, **14**, 2718 (2002).
16. P. Lobitz, H. Fullbier, A. Reiche, J. C. Illner, H. Reuter, and S. Horing, *Solid State Ionics*, **58**, 41 (1992).
17. F. Alloin, J.-Y. Sanchez, and M. Armand, *Electrochim. Acta*, **37**, 1729 (1992).
18. J. Saunier, F. Alloin, and J.-Y. Sanchez, *Electrochim. Acta*, **45**, 1255 (2000).
19. K. Jankova, P. Jannasch, and S. Hvilsted, *J. Mater. Chem.*, **14**, 2902 (2004).
20. L. L. Ionescu-Vasii, Y. Abu-Lebdeh, and M. Armand, *Solid State Ionics*, **176**, 2769 (2005).
21. J. Huang, Z.-Z. Tong, B. Zhou, J.-T. Xu, and Z.-Q. Fan, *Polymer*, **54**, 3098 (2013).
22. N. P. Young, D. Devaux, R. Khurana, G. W. Coates, and N. P. Balsara, *Solid State Ionics*, **263**, 87 (2014).
23. L. Leibler, *Macromolecules*, **13**, 1602 (1980).
24. M. W. Matsen and R. B. Thompson, *J. Chem. Phys.*, **111**, 7139 (1999).
25. M. W. Matsen, *J. Chem. Phys.*, **113**, 5539 (2000).
26. T. Niitani, M. Shimada, K. Kawamura, and K. Kanamura, *Journal of Power Sources*, **146**, 386 (2005).
27. T. Niitani, M. Amaike, H. Nakano, K. Dokko, and K. Kanamura, *J. Electrochem. Soc.*, **156**, A577 (2009).
28. M. Singh, O. Odusanya, G. M. Wilmes, H. B. Eitouni, E. D. Gomez, A. J. Patel, V. L. Chen, M. J. Park, P. Fragouli, H. Iatrou, N. Hadjichristidis, D. Cookson, and N. P. Balsara, *Macromolecules*, **40**, 4578 (2007).
29. R. Bouchet, T. N. T. Phan, E. Beaudoin, D. Devaux, P. Davidson, D. Bertin, and R. Denoyel, *Macromolecules*, **47**, 2659 (2014).
30. A. Panday, S. Mullin, E. D. Gomez, N. Wanakule, V. L. Chen, A. Hexemer, J. Pople, and N. P. Balsara, *Macromolecules*, **42**, 4632 (2009).
31. E. D. Gomez, A. Panday, E. H. Feng, V. Chen, G. M. Stone, A. M. Minor, C. Kisielowski, K. H. Downing, O. Borodin, G. D. Smith, and N. P. Balsara, *Nano Letters*, **9**, 1212 (2009).
32. R. Yuan, A. A. Teran, I. Gurevitch, S. A. Mullin, N. S. Wanakule, and N. P. Balsara, *Macromolecules*, **46**, 914 (2013).
33. I. Villaluenga, X. C. Chen, D. Devaux, D. T. Hallinan, and N. P. Balsara, *Macromolecules* **48**, 358 (2015).
34. W. S. Young and T. H. Epps, *Macromolecules*, **42**, 2672 (2009).
35. A. A. Teran and N. P. Balsara, *J. Phys. Chem. B*, **118**, 4 (2014).
36. S. A. Mullin, G. M. Stone, A. Panday, and N. P. Balsara, *J. Electrochem. Soc.*, **158**, A619 (2011).
37. D. H. C. Wong, J. L. Thelen, Y. Fu, D. Devaux, A. A. Pandya, V. S. Battaglia, N. P. Balsara, and J. M. DeSimone, *Proc. Natl. Acad. Sci. U. S. A.*, **111**, 3327 (2014).
38. N. P. Balsara and J. Newman, *J. Chem. Educ.*, **90**, 446 (2013).
39. S. Sylla, J.-Y. Sanchez, and M. Armand, *Electrochim. Acta*, **37**, 1699 (1992).
40. D. T. Hallinan, S. A. Mullin, G. M. Stone, and N. P. Balsara, *J. Electrochem. Soc.*, **160**, A464 (2013).
41. G. M. Stone, S. A. Mullin, A. A. Teran, D. T. Hallinan, A. M. Minor, A. Hexemer, and N. P. Balsara, *J. Electrochem. Soc.*, **159**, A222 (2012).
42. G. P. Bierwagen, *Electrochim. Acta*, **37**, 1471 (1992).
43. I. Yoshimatsu, T. Hirai, and J. Yamaki, *J. Electrochem. Soc.*, **135**, 2422 (1988).
44. J.-N. Chazalviel, *Phys. Rev. A*, **42**, 7355 (1990).
45. K. Kanamura, S. Shiraishi, H. Tamura, and Z.-i. Takehara, *J. Electrochem. Soc.*, **141**, 2379 (1994).
46. C. Fringant, A. Tranchant, and R. Messina, *Electrochim. Acta*, **40**, 513 (1995).
47. D. Aurbach and Y. Cohen, *J. Electrochem. Soc.*, **143**, 3525 (1996).

48. D. Aurbach, E. Zinigrad, Y. Cohen, and H. Teller, *Solid State Ionics*, **148**, 405 (2002).
49. E. Eweka, J. R. Owen, and A. Ritchie, *J. Power Sources*, **65**, 247 (1997).
50. T. Tatsuma, M. Taguchi, and N. Oyama, *Electrochim. Acta*, **46**, 1201 (2001).
51. C. Brissot, M. Rosso, J.-N. Chazalviel, and S. Lascaud, in *Stud. Surf. Sci. Catal.*, N. Oyama, Y. Iwasawa, and K. Hironobu Editors, p. 947, Elsevier (2001).
52. M. Rosso, T. Gobron, C. Brissot, J.-N. Chazalviel, and S. Lascaud, *J. Power Sources*, **97–98**, 804 (2001).
53. A. Teyssot, C. Belhomme, R. Bouchet, M. Rosso, S. Lascaud, and M. Armand, *J. Electroanal. Chem.*, **584**, 70 (2005).
54. C. Naudin, J. L. Bruneel, M. Chami, B. Desbat, J. Grondin, J. C. Lassègues, and L. Servant, *J. Power Sources*, **124**, 518 (2003).
55. C. Monroe and J. Newman, *J. Electrochem. Soc*, **150**, A1377 (2003).
56. F. Orsini, A. du Pasquier, B. Beaudouin, J.-M. Tarascon, M. Trentin, N. Langenhuizen, E. d. Beer, and P. Notten, *J. Power Sources*, **81–82**, 918 (1999).
57. L. Gireaud, S. Grugeon, S. Laruelle, B. Yrieix, and J.-M. Tarascon, *Electrochem. Commun.*, **8**, 1639 (2006).
58. C. M. Lopez, J. T. Vaughey, and D. W. Dees, *J. Electrochem. Soc.*, **156**, A726 (2009).
59. H. Honbo, K. Takei, Y. Ishii, and T. Nishida, *J. Power Sources*, **189**, 337 (2009).
60. S. Liu, N. Imanishi, T. Zhang, A. Hirano, Y. Takeda, O. Yamamoto, and J. Yang, *J. Electrochem. Soc.*, **157**, A1092 (2010).
61. S. Liu, N. Imanishi, T. Zhang, A. Hirano, Y. Takeda, O. Yamamoto, and J. Yang, *J. Power Sources*, **195**, 6847 (2010).
62. R. Bhattacharyya, B. Key, H. Chen, A. S. Best, A. F. Hollenkamp, and C. P. Grey, *Nature Mater.*, **9**, 504 (2010).
63. H. Sano, H. Sakaebe, and H. Matsumoto, *J. Power Sources*, **196**, 6663 (2011).
64. X. H. Liu, L. Zhong, L. Q. Zhang, A. Kushima, S. X. Mao, J. Li, Z. Z. Ye, J. P. Sullivan, and J. Y. Huang, *Appl. Phys. Lett.*, **98**, 183107 (2011).
65. H. Ghassemi, M. Au, N. Chen, P. A. Heiden, and R. S. Yassar, *Appl. Phys. Lett.*, **99**, 123113 (2011).
66. S. Chandrashekar, N. M. Trease, H. J. Chang, L.-S. Du, C. P. Grey, and A. Jerschow, *Nature Mater.*, **11**, 311 (2012).
67. M. Z. Mayers, J. W. Kaminski, and T. F. Miller, *J. Phys. Chem. C*, **116**, 26214 (2012).
68. S.-H. Kim, K.-H. Choi, S.-J. Cho, E.-H. Kil, and S.-Y. Lee, *J. Mater. Chem. A*, **1**, 4949 (2013).
69. R. Khurana, J. L. Schaefer, L. A. Archer, and G. W. Coates, *J. Am. Chem. Soc.*, **136**, 7395 (2014).
70. W. Xu, J. Wang, F. Ding, X. Chen, E. Nasybulin, Y. Zhang, and J.-G. Zhang, *Energ. Environ. Sci.*, **7**, 513 (2014).
71. K. J. Harry, D. T. Hallinan, D. Y. Parkinson, A. A. MacDowell, and N. P. Balsara, *Nature Mater.*, **13**, 69 (2014).
72. N. S. Schauser, K. J. Harry, D. Y. Parkinson, H. Watanabe, and N. P. Balsara, *J. Electrochem. Soc.*, **162**, A398 (2015).
73. C. Monroe and J. Newman, *J. Electrochem. Soc.*, **152**, A396 (2005).
74. A. A. MacDowell, D. Y. Parkinson, A. Haboub, E. Schaible, J. R. Nasiatka, C. A. Yee, J. R. Jameson, J. B. Ajo-Franklin, C. R. Brodersen, and A. J. McElrone, *Proc. SPIE*, **8506**, 850618 (2012).
75. C. Delacourt, L. Laffont, R. Bouchet, C. Wurm, J.-B. Leriche, M. Morcrette, J.-M. Tarascon, and C. Masquelier, *J. Electrochem. Soc.*, **152**, A913 (2005).
76. V. Srinivasan and J. Newman, *J. Electrochem. Soc.*, **151**, A1517 (2004).
77. F. Croce, S. Sacchetti, and B. Scrosati, *J. Power Sources*, **162**, 685 (2006).
78. F. Maia, A. MacDowell, S. Marchesini, H. A. Padmore, D. Y. Parkinson, J. Pien, A. Schirotzek, and C. Yang, *Proc. SPIE*, **7800**, 78000F (2010).
79. A. K. Padhi, K. S. Nanjundaswamy, and J. B. Goodenough, *J. Electrochem. Soc.*, **144**, 1188 (1997).